


Technique for studying in high resolution poromechanical deformation of a rocklike medium

Arnold Bachrach* and Yaniv Edery†

Faculty of Civil and Environmental Engineering, Technion, Haifa, Israel (Received 13 November 2022; revised 21 March 2023; accepted 6 July 2023; published 4 August 2023)

Pressurized fluid injection into underground rocks occurs in applications like carbon sequestration, hydraulic fracturing, and wastewater disposal and may lead to human-induced earthquakes and surface uplift. The fluid injection raises the pore pressure within the porous rocks, while deforming them, yet this coupling is rarely captured by experiments. Moreover, experimental studies of rocks are usually limited to postmortem inspection and cannot capture the complete deformation process in time and space. In this Letter we will present a unique experimental system that can capture the spatial distribution of poromechanical effects in real time by using an artificial rocklike transparent medium mimicking the deformation of sandstone. We will demonstrate the system abilities through a fluid injection experiment, showing the nonuniform poroelastic expansion of the medium and the corresponding poroelastic model that captures completely the results without any fitting parameters. Moreover, our results demonstrate and validate the underlying assumptions of the poroelastic theory for fluid injection in rocklike materials, which are relevant for understanding human-induced earthquakes and injection induced surface uplift.

DOI: [10.1103/PhysRevE.108.L022901](https://doi.org/10.1103/PhysRevE.108.L022901)**I. INTRODUCTION**

In recent years the study of poromechanics has proved to be seminal for understanding the environmental effects of fluid injections into the underground, as occurs in carbon sequestration [1,2], hydraulic fracturing [3], enhanced geothermal energy production [4], and wastewater disposal [5–7]. The fluid injection raises the pore pressure within the underground rocks while deforming them, leading to human-induced earthquakes [5–10] and surface uplift [5,7,11]. While human-induced earthquakes are attributed to fault reactivation [8–10], surface uplift is a phenomenon that can be attributed to poromechanical expansion of the underground rocks [5,12,13]. Moreover, the poromechanical response of the medium to fluid injection can induce underground stresses and facilitate fault reactivation [14,15].

Early observations on the coupling of flow, pore pressure, and deformation have been documented by King (1892) [16], as he measured water-level fluctuations in wells due to passing trains. The weight of the train elastically compresses the underground aquifer, hence raising its pore pressure and elevating the surrounding well's water level [17]. These observations were accompanied by comprehensive scientific study, mainly in the context of soil consolidation [18,19] and elastic storage in a confined aquifer [20–22], formulating the theory of poroelasticity [18,19,23].

Originally, the poroelastic theory was developed for the case of fluid outflow from the porous medium, whether by loading or by fluid extraction, hence experiments that prove and demonstrate the validity of this theory for fluid

injection scenarios are rare. In recent years few injection experiments on soft or loosely consolidated materials [24–27] provided meaningful insight on poromechanical effects, yet these materials exhibit properties which are very different from real rocks as their solid internal structure, mechanical behavior, and permeability. Experiments on real rocks are usually limited to postmortem inspection (e.g., [28,29]) and hence cannot capture the poroelastic reversible effects nor the complete spatial-temporal phenomena [25].

In this Letter, we will present an experimental system for studying spatial distribution of poromechanical effects in real time using a unique rocklike transparent medium that mimics the deformation of sandstone. We will use our experimental system for quantifying and proving the nonuniform poroelastic expansion of the artificial rocks due to fluid injection, a phenomenon that we fully model using the theory of poroelasticity [18,19,23].

II. METHODS

Our experimental system is based on a transparent artificial rock, made from sintered PMMA (polymethyl methacrylate) beads with a mean diameter of 78 microns, measured using a dynamic light scattering (DLS) test (see Figs. S1a and S1b in the Supplemental Material [30]). We chemically sinter the beads inside a PMMA chamber using an acetone mixture that dissolves the edges of the beads and subsequently drain the mixture, allowing the beads to solidify together into a rocklike porous material [see Fig. 1(a), and Fig. S1c in the Supplemental Material [30]]. In the specific injection experiment presented here, the sample edge is fixed by an epoxy glue to the flow cell inlet, while its other edge remains free [Fig. 1(a)]. The artificial rock porosity, $n = 0.43$, is measured from microcomputed tomography (micro-CT) scan

*Arnoldbachrach@gmail.com

†Yanivedery@gmail.com

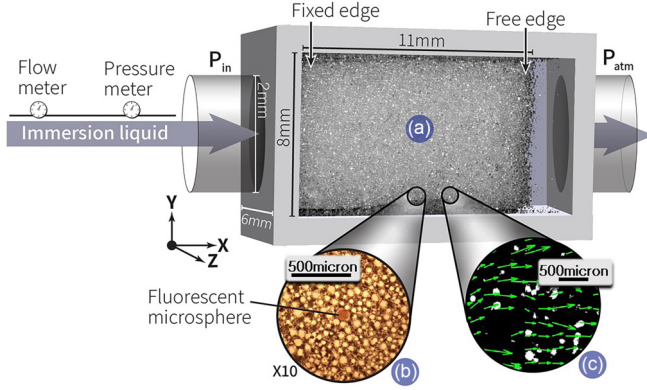


FIG. 1. Experimental setup. (a) The artificial rocklike sample within the flow cell, where the injection point is fixed to the flow-cell wall while the outlet edge remains free. (b) The sintered PMMA beads with the fluorescent microspheres forming the artificial rock, as seen under optical microscope. (c) PIV analysis of the fluorescent microsphere's movement [34] provides the whole displacement field within the sample.

of the sample (Fig. S1d in the Supplemental Material [30]) as the ratio between black (voids) and the overall number of pixels over the binarized scanned volume. The artificial rock's permeability, $k = 4.5 \times 10^{-12} \text{ m}^2$, is measured using Darcy's law over the measured pressure difference and the measured discharge, and also by the Kozeny-Carman equation [31,32], using the mean grain diameter from the DLS test as a representative grain size, which provides a similar value, $k = 5.85 \times 10^{-12} \text{ m}^2$. These values of permeability correspond to a high-permeability sandstone [33].

To track the local deformation, we incorporate and solidify 1.2% (by weight) fluorescent polyethylene microspheres (106–125 microns in diameter) within the sample [Fig. 1(b)]. Then, we saturate the sample with oil (Cargille immersion liquid) that has a refractive index matching the PMMA ($RI = 1.49$), transforming the sample from opaque to transparent, apart from the fluorescent microspheres. The fluorescent microspheres are excited by 460 nm LED light and emit at a range 580–700 nm, which is filtered by a long-pass 625-nm filter [Fig. 1(c)].

The oil flow through the artificial rock is driven by a pressure difference using a pressure pump (Fluigent-LU-FEZ-7000) as we monitor the inlet pressure and fluid discharge by a pressure sensor (Fluigent-EIPS7000) and flow meter (Fluigent-FLU-XL), respectively. This pressure difference increases by 70 mbar/sec as we track the deformation by the fluorescent microspheres movement using a 4 Mpx camera (Phantom-v2640) at a rate of 100 frames per second at 12 bits. A particle image velocimetry (PIV) software (PIVLAB 2.50) [34] provides the whole displacement field within the sample for each time step by analyzing the fluorescent microsphere's joint movement [Fig. 1(c), and Fig. S2 in the Supplemental Material [30]]. We calculated the PIV accuracy as 0.57 microns (0.04 pixels) by applying the analysis on the system without any pressure difference, where the displacement of the fluorescent beads is zero.

III. RESULTS

The embedded fluorescent microsphere movement in the artificial rock allows us to calculate the displacements within the sample using the PIV software [34] for each inlet pressure that drives the flow. By addressing the displacement of the sample's free edge, a pseudo-stress-strain curve as in a rheological test can be derived [Fig. 2(a)]. In Fig. 2(a), the x axis is the sample's free edge displacement averaged over the y axis of the sample and normalized by the sample's initial length, thus providing the overall strain of the sample. The y axis in Fig. 2(a) is the inlet (gauge) pressure, representing the stress in the pseudo-stress-strain curve. Looking at the curve, we identify a trend similar to that of a pulled rock in a tensile test: Linear extension for pressures of up to 0.084 MPa, followed by a nonlinear extension. Moreover, the normalized extension of our sample is on the same scale as a pulled sandstone strain in a pulling test [Fig. 2(b)] [35]. We verify the pseudo-stress-strain curve transition from elastic to plastic by a cyclic pressure test [Fig. 2(c)], where we apply cycles of pressure increase followed by a pressure decrease, with an increasingly higher pressure for each cycle. As seen in Fig. 2(c), the strain at cycle 1, reaching about 0.1 Mpa, is completely reversible, meaning that the deformation is elastic and nondissipating. However, in the following cycles, we can see a larger and larger remnant strain, manifested in the hysteresis of the cycle, meaning that indeed a plastic component is added to the deformation.

Our artificial rock simulates real rock deformation [35] by moving from the elastic to the elastoplastic regime. However, unlike opaque rocks, it allows us to quantify the coupling between the pressurized flow and the deformation by analyzing the internal local displacement as the pressure drops from inlet to outlet. We analyze the internal displacement of the experiment in Fig. 2(a) by calculating the mean displacement over the sample's y axis for each inlet pressure, with a resolution of 224 microns along x . Figure 3 shows the measured displacement along the sample for three different inlet pressures, all from the elastic regime of the same experiment. As can be seen, the increase in displacement along x is not distinctly linear as one would expect from the analogy to a pulling test, suggesting a nonuniform strain distribution. To model this poroelastic expansion, we use the theory of poroelasticity, which combines Hooke's law, Darcy's law, and Terzaghi's concept of effective stress [19,23,36]. The latter coincides with Biot's theory of consolidation [18] for incompressible fluid and grains.

The pore Reynolds number along the experiment has been calculated to be < 0.1 , hence the flow through the porous medium should be governed by Darcy's law [32,37]. Our boundary conditions confined the flow to the x direction, allowing us to use the one-dimensional Darcy's law that relates the pore pressure drop ($\frac{dp}{dx}$) with the fluid flux (q), through the permeability (k) and the dynamic viscosity of the fluid ($\mu = 11.7 \text{ mPa}\cdot\text{s}$):

$$\frac{dp}{dx} = -\frac{\mu}{k} q. \quad (1)$$

There is however some flow in the y direction, limited to the inlet and to the outlet area, since the inlet and outlet

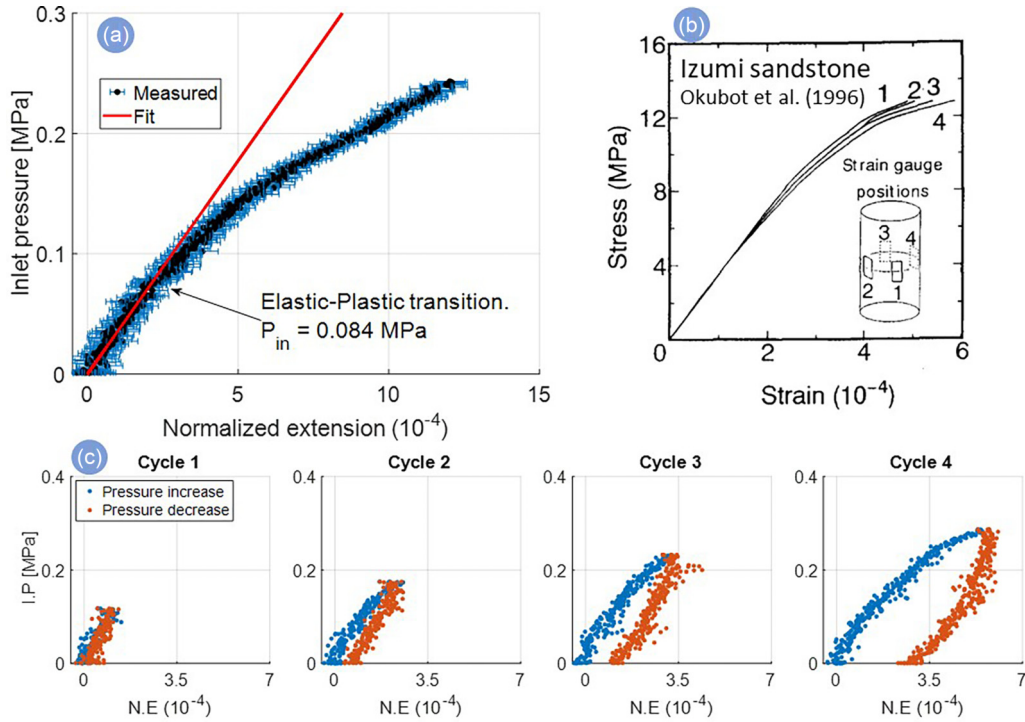


FIG. 2. Pseudo-stress-strain curves. (a) The strain is the total extension normalized by the sample’s initial length, and the stress is the measured inlet pressure. The curve follows the same transition between elastic to plastic deformation observed in a pulled rock. (b) Comparison of our results to a sandstone pulling test done by Okubot *et al.* [35]. The extension of our sample is similar not only in the general trend but also in the scale of strain. (c) Cyclic pressure tests, where the end pressure applied on the sample increases on every cycle, and subsequently decreases. The strain at cycle 1 reaching about 0.1 MPa is completely reversible, indicating an elastic response, however, the following cycles with higher end pressure are not reversible, showing a remnant plastic strain manifested by each cycle hysteresis. The sample in the cyclic test is slightly stronger than the sample in inset (a) due to slight variation in the sintering process. I.P: Inlet pressure, N.E: Normalized extension.

pipe cross section (the pipe measurements are 4 mm o.d., 2 mm i.d.) is smaller than the flow cell cross section by about one order of magnitude [Fig. 1(a)]. This nonuniformity has some local effect on the deformation, but as we study here the average (along y) behavior of the medium, we will neglect this effect in the current work.

Due to the small elastic deformations of the artificial rock [Fig. 2(a)], the change in porosity measured from the sample’s elongation is negligible ($<0.1\%$), hence we will treat the permeability as a constant, which means that while the pore pressure strains the medium, the deformation has a negligible

effect on the flow. According to linear elasticity, the material response for an applied stress (or pressure in our case) is instantaneous [38]; as such, for each inlet pressure we apply, the system can be regarded as a steady state with a constant flux along the sample ($\frac{dq}{dx} = 0$).

Since q , k , and μ are assumed to be constants, the pore pressure will drop linearly along the sample. Under the conditions $p(x = 0) = p_{injection}$ and $p(x = L) = p_{atm}$ for a sample at length L , the pore pressure along the sample will be

$$p(x) = -\frac{p_{in}}{L}x + p_{in} . \tag{2}$$

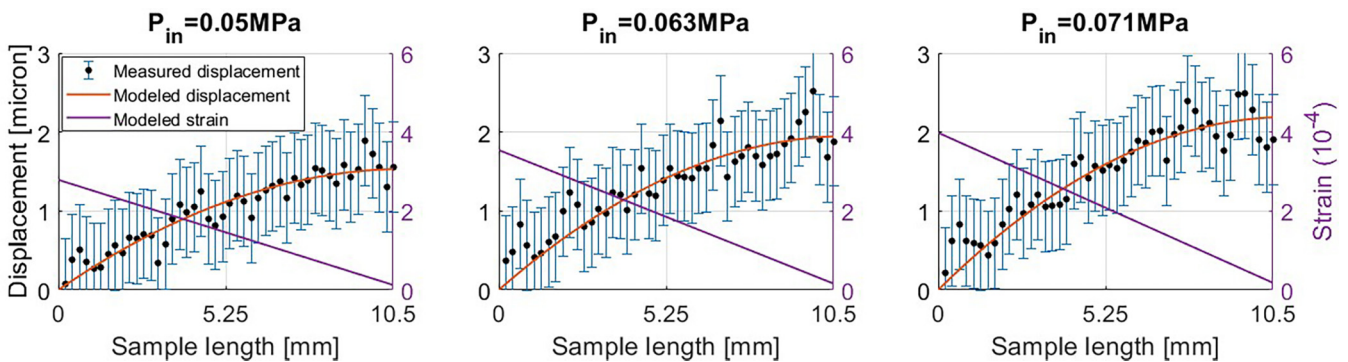


FIG. 3. Internal displacement along the sample. The poroelastic model (brown curve) predicts accurately the measured displacement (black dots), without any fitting parameters. Using the model, we also calculate the internal strain (purple curve), which decreases linearly along the medium, following the pore pressure. While the injection area is strongly expanding, the sample’s far edge hardly strains.

Although the sample is extending like in a pulling test (Fig. 2), the boundary conditions are those of the Oedometric test [39,40], where the sample is compressed vertically while confined laterally. The pore pressure acts as a normal tensional stress in the same way a confined pressure acts, but in the opposite direction (in line with the concept of effective stress) [19,23,36], yet, our setup allows the sample to expand only in the x direction, while both y and z directions are constrained by the flow-cell walls (see Fig. 1 for orientation), so there is one direction of stress (σ_x) and free strain (e_x) and two other directions of no strain ($e_y = e_z = 0$) and reaction stresses (σ_y, σ_z), just like in the Oedometric test. Using these boundary conditions with Hook's law for an isotropic elastic body, addressing the presence of fluid through the concept of effective stress [19,23,36] leads to the following relation (see the Supplemental Material [30] for the full derivation):

$$e_x = \frac{du}{dx} = \frac{1}{E_{\text{oed}}} p, \quad (3)$$

where u is the displacement in the x direction and E_{oed} is the Oedometric modulus [40]. Substituting Eq. (2) in Eq. (3) gives

$$e_x = \frac{du}{dx} = \frac{1}{E_{\text{oed}}} \left(-\frac{p_{\text{in}}}{L} x + p_{\text{in}} \right). \quad (4)$$

Under the condition that the inlet boundary is fixed [$u(x=0) = 0$], we integrate (4) to derive a solution for the displacement at each location along the x axis:

$$u(x) = -\frac{p_{\text{in}}}{2E_{\text{oed}}L} x^2 + \frac{p_{\text{in}}}{E_{\text{oed}}} x. \quad (5)$$

Applying Eq. (5) on the sample's edge ($x = L$) we can write

$$p_{\text{in}} = 2E_{\text{oed}} \frac{u_{\text{edge}}}{L}. \quad (6)$$

Equation (6) suggests that when the one-dimensional strain (u_{edge}/L) is caused by pore pressure instead of external force, the sample's edge will displace as if the material is twice as stiff as in a regular Oedometric test. This is due to the fact that in a regular Oedometric test the stress is constant along the medium, while here the effective stress follows the pore pressure and hence decreases along the sample. Moreover, $2E_{\text{oed}}$ is exactly the slope of our pseudo-stress-strain curve [Fig. 2(a), red line]. Hence, from the slope of the measured pseudo-stress-strain curve we can directly calculate E_{oed} . Knowing the value of E_{oed} , we can use Eq. (5) to model the displacement in each point along our sample for all the inlet pressures and without any fitting parameters (Fig. 3, brown line). As can be seen in Fig. 3, the model agrees extremely well with

the measured data. Knowing the value of E_{oed} , Eq. (3) can be used for calculating the strain along the sample (Fig. 3, purple line). Following the pore pressure, the strain decreases linearly along the sample. While the injection area is highly expanding, the outlet area hardly strains.

IV. CONCLUSION

In this study we use a unique rocklike medium together with an advanced experimental system to visualize the internal displacement field induced by pressurized flow through the porous medium. We show that one-dimensional (1D) fluid injection induces linear decreasing expansion, which leads to a parabolic increase in the cumulative displacement along the medium, a phenomenon that we modeled accurately without any fitting parameters using the poroelastic theory. The main contribution of this study is the ability to track the complete spatial-temporal poroelastic expansion of rocklike materials. The results emphasize that both the scale and the trends of our porous medium deformation are similar to that of real rocks, and in line with the poroelastic theory. Hence, our methods can be used to study in detail the poromechanics of rocks in the laboratory for different scenarios and boundary conditions.

As a transparent 3D-porous medium with realistic grain size, our artificial rocks can also be used for studying flow and transport in rocks and soils, and as a reference for numerical simulations that can be done directly on the artificial rocks' micro-CT scans [41].

Note that the Oedometric modulus we mentioned in the 1D model can be further used for the natural boundary conditions of a confined aquifer with one direction of free strain (i.e., the surface) and two other directions of zero strain (i.e., the underground).

In future studies we intend to focus on the development of cracks and compaction bands in the artificial rocks due to fluid injection, in order to get a better understating of the poromechanical effects that fluid injections into the underground have on the surrounding rocks.

ACKNOWLEDGMENTS

We thank A. Guadagnini and G. Dellavecchia for their insightful comments and discussions. We also thank L. Abezgauz, S. Sulieman, and M. Stolar for their help in the experiments. A.B. acknowledges The Nancy and Stephen Grand Technion Energy Program (GTEP) for supporting this research. Y.E. and A.B. acknowledge that this research was supported by the ISF-NSFC joint research program (Grant No. 3333/19).

[1] S. Ó Snæbjörnsdóttir, B. Sigfússon, C. Marieni, D. Goldberg, S. R. Gislason, and E. H. Oelkers, Carbon dioxide storage through mineral carbonation, *Nat. Rev. Earth Environ.* **1**, 90 (2020).
 [2] M. D. Zoback and S. M. Gorelick, Earthquake triggering and large-scale geologic storage of carbon dioxide, *Proc. Natl. Acad. Sci. USA* **109**, 10164 (2012).

[3] X. Bao and D. W. Eaton, Fault activation by hydraulic fracturing in western Canada, *Science*, **354**, 1406 (2016).
 [4] N. Deichmann and D. Giardini, Earthquakes induced by the stimulation of an enhanced geothermal system below Basel (Switzerland), *Seismol. Res. Lett.* **80**, 784 (2009).
 [5] M. Shirzaei, W. L. Ellsworth, K. F. Tiampo, P. J. González, and M. Manga, Surface uplift and time-dependent seismic

- hazard due to fluid injection in eastern Texas, *Science* **353**, 1416 (2016).
- [6] S. Horton, Disposal of hydrofracking waste fluid by injection into subsurface aquifers triggers earthquake swarm in central arkansas with potential for damaging earthquake, *Seismol. Res. Lett.* **83**, 250 (2012).
- [7] D. Juncu *et al.*, Injection-induced surface deformation and seismicity at the Hellisheidi geothermal field, Iceland, *J. Volcanol. Geotherm. Res.* **391**, 106337 (2020).
- [8] W. L. Ellsworth, Injection-Induced Earthquakes, *Science*, **341**, 1225942 (2013).
- [9] S. Cesca *et al.*, Seismicity at the Castor gas reservoir driven by pore pressure diffusion and asperities loading, *Nat. Commun.* **12**, 4783 (2021).
- [10] F. Cappa, Y. Guglielmi, and L. de Barros, Transient evolution of permeability and friction in a slowly slipping fault activated by fluid pressurization, *Nat. Commun.* **13**, 3039 (2022).
- [11] T. Onuma and S. Ohkawa, Detection of surface deformation related with CO₂ injection by DInSAR at In Salah, Algeria, in *Energy Procedia*, edited by J. Gale, H. Herzog, and J. Braitsch (Elsevier, Washington DC, USA, 2009), Vol. 1, pp. 2177–2184.
- [12] Z. R. Chen, Poroelastic model for induced stresses and deformations in hydrocarbon and geothermal reservoirs, *J. Pet. Sci. Eng.* **80**, 41 (2011).
- [13] I. D. Palmer, Uplifts and Tilts at Earth's Surface Induced by Pressure Transients From Hydraulic Fractures, *SPE Production Eng.* **5**, 324 (1990).
- [14] K. W. Chang and P. Segall, Injection-induced seismicity on basement faults including poroelastic stressing, *J. Geophys. Res. Solid Earth* **121**, 2708 (2016).
- [15] P. Segall and S. Lu, Injection-induced seismicity: Poroelastic and earthquake nucleation effects, *J. Geophys. Res. Solid Earth* **120**, 5082 (2015).
- [16] F. King, Observations and experiments on the fluctuations in the level and rate of movement of ground-water on the wisconsin agricultural experiment station farm, Bulletin No. 5, U.S. Department of Agriculture, Washington, 1892.
- [17] C. E. Jacob, Fluctuations in Artesian Pressure produced by passing railroad-trains as shown in a well on Long Island, New York, *Trans., Am. Geophys. Union* **20**, 666 (1939).
- [18] M. A. Biot, General theory of three-dimensional consolidation, *J. Appl. Phys.* **12**, 155 (1941).
- [19] K. Terzaghi, R. B. Peck, and G. Mesri, *Soil Mechanics in Engineering Practice* (John Wiley & Sons, U.S., 1962).
- [20] C. E. Jacob, On the flow of water in an elastic artesian aquifer, *Eos Trans. AGU* **21**, 574 (1940).
- [21] O. E. Meinzer, Compressibility and elasticity of artesian aquifers, *Eco. Geology* **23**, 263 (1928).
- [22] C. v. Theis, The significance and nature of the cone of depression in ground-water bodies, *Eco. Geology* **33**, 889 (1938).
- [23] H. F. Wang, *Theory of Linear Poroelasticity with Applications to Geomechanics and Hydrogeology* (Princeton University Press, Princeton, 2017).
- [24] D. R. Hewitt, J. S. Nijjer, M. G. Worster, and J. A. Neufeld, Flow-induced compaction of a deformable porous medium, *Phys. Rev. E* **93**, 023116 (2016).
- [25] C. W. MacMinn, E. R. Dufresne, and J. S. Wettlaufer, Fluid-driven Deformation of a Soft Granular Material, *Phys. Rev. X* **5**, 011020 (2015).
- [26] K. H. Parker, R. v. Mehta, and C. G. Caro, Steady flow in porous, elastically deformable materials. http://asmedigitalcollection.asme.org/appliedmechanics/article-pdf/54/4/794/5459498/794_1.pdf (1987).
- [27] Y. Lanir, S. Sauob, and P. Maretsky, Nonlinear finite deformation response of open cell polyurethane sponge to fluid filtration, http://asmedigitalcollection.asme.org/appliedmechanics/article-pdf/57/2/449/5460912/449_1.pdf (1990).
- [28] M. King *et al.* Mechanics of hydraulic fracturing, <http://onepetro.org/trans/article-pdf/210/01/153/2176767/spe-686-g.pdf> (1956).
- [29] B. Bohloli and C. J. de Pater, Experimental study on hydraulic fracturing of soft rocks: Influence of fluid rheology and confining stress, *J. Pet. Sci. Eng.* **53**, 1 (2006).
- [30] See Supplemental Material at <http://link.aps.org/supplemental/10.1103/PhysRevE.108.L022901> for equation derivation and methodology, which includes Ref. [42].
- [31] R. A. Freeze and J. A. Cherry, *Groundwater* (Prentice-Hall, Englewood Cliffs, NJ, 1979).
- [32] J. Bear, *Dynamics of Fluids in Porous Media* (Dover, New York, 1988).
- [33] J. C. Jaeger, N. G. Cook and R. Zimmerman, *Fundamentals of Rock Mechanics* (Blackwell Publishing, Singapore, 2007).
- [34] W. Thielicke and R. Sonntag, Particle image velocimetry for matlab: Accuracy and enhanced algorithms in PIVlab, *J. Open Res. Softw.* **9**, 12 (2021).
- [35] S. Okubo and K. Fukui, Complete stress-strain curves for various rock types in uniaxial tension, *Int. J. Rock Mech. Min. Sci. Geomech. Abstr.* **33**, 549 (1996).
- [36] A. Nur and J. D. Byerlee, An exact effective stress law for elastic deformation of rock with fluids, *J. Geophys. Res.* **76**, 6414 (1971).
- [37] W. Sobieski and A. Trykozko, Darcy's and Forchheimer's laws in practice. Part I. the experiment, *Tech. Sci.* **17**, 321 (2014).
- [38] W. D. Means, *Stress and Strain* (Springer, New York, 1976).
- [39] R. Castellanza and R. Nova, Oedometric tests on artificially weathered carbonatic soft rocks, *J. Geotechnical Geoenvironmental Eng.* **130**, 728 (2004).
- [40] A. Sawicki and W. Swidzinski, Elastic moduli of non-cohesive particulate materials, *Powder Technol.* **96**, 24 (1998).
- [41] J. Yang, J. Crawshaw, and E. S. Boek, Quantitative determination of molecular propagator distributions for solute transport in homogeneous and heterogeneous porous media using lattice Boltzmann simulations, *Water Resour. Res.* **49**, 8531 (2013).
- [42] N. Otsu, A threshold selection method from gray-level histograms, *IEEE Trans. Syst. Man Cybern.* **9**, 62 (1979).